

# Micro-poro-elasticity of baghdadite-based bone tissue engineering scaffolds: A unifying approach based on ultrasonics, nanoindentation, and homogenization theory

Hawraa Kariem<sup>a</sup>, Maria-Ioana Pastrama<sup>a</sup>, Seyed Iman Roohani-Esfahani<sup>b</sup>, Peter Pivonka<sup>c</sup>, Hala Zreiqat<sup>b</sup>, Christian Hellmich<sup>a,\*</sup>

<sup>a</sup> Institute for Mechanics of Materials and Structures, Vienna University of Technology (TU Wien), Karlsplatz 13/E202, A-1040 Vienna, Austria

<sup>b</sup> Biomaterials and Tissue Engineering Research Unit, School of AMME, The University of Sydney, Sydney 2006, Australia

<sup>c</sup> Australian Institute for Musculoskeletal Science, NorthWest Academic Centre, Department of Medicine, University of Melbourne, Victoria 3021, Australia

## ARTICLE INFO

### Article history:

Received 5 August 2014

Received in revised form 21 October 2014

Accepted 27 October 2014

Available online 28 October 2014

### Keywords:

Scaffold

Baghdadite

Nanoindentation

Ultrasound

Micromechanics

## ABSTRACT

Microstructure–elasticity relations for bone tissue engineering scaffolds are key to rational biomaterial design. As a contribution thereto, we here report comprehensive length measuring, weighing, and ultrasonic tests at 0.1 MHz frequency, on porous baghdadite ( $\text{Ca}_3\text{ZrSi}_2\text{O}_9$ ) scaffolds. The resulting porosity–stiffness relations further confirm a formerly detected, micromechanically explained, general relationship for a great variety of different polycrystals, which also allows for estimating the zero-porosity case, i.e. Young modulus and Poisson ratio of pure (dense) baghdadite. These estimates were impressively confirmed by a physically and statistically independent nanoindentation campaign comprising some 1750 indents. Consequently, we can present a remarkably complete picture of porous baghdadite elasticity across a wide range of porosities, and, thanks to the micromechanical understanding, reaching out beyond classical elasticity, towards poroelastic properties, quantifying the effect of pore pressure on the material system behavior.

© 2014 The Authors. Published by Elsevier B.V. This is an open access article under the CC BY-NC-ND license (<http://creativecommons.org/licenses/by-nc-nd/4.0/>).

## 1. Introduction

With an estimated 2.2 million yearly bone graft procedures for the treatment of critical size defects, bone is the second-most implanted material after blood [1]. Despite considerable progress over the years, the current gold standard, autografting [2], where bone from the patient is transplanted from one place to another, is limited by the amount of bone available, and may imply pre- and post-operative complications and morbidity, as well as the risk of infection [3]. The current clinical alternative, allografting, where cadaveric or synthetic bone is implanted, carries the risk of viral disease transmission, immunogenicity, and non-union [4]. This has motivated, for more than two decades, research in the field of bone tissue engineering [5–8], aiming at repairing damaged bone and restoring its functions [9] with the help of biocompatible materials cultivated with cells and corresponding growth factors [10]. Therefore, the scaffolds have to be designed in a way to provide sufficient porosity for good vascular and tissue ingrowth, while not overly compromising the overall mechanical properties of the implant, i.e. its stiffness and strength. This design process, involving also the biological properties of the implant material, turns out as very complex, and

implies many design parameters whose interplay is extremely challenging to decipher in a classical ‘trial-and-error’ procedure, requiring a sheer innumerable multitude of in vitro and in vivo experiments. This challenging situation has given rise to the wish for rational, computer-aided design of biomaterials, regarding not only biological and cell transport aspects, but also mechanics. The present paper will concentrate on the latter aspect, thereby not being restricted to the measurement of some mechanical properties, but to a micromechanics theory-based understanding of an entire class of ceramic biomaterials, supported by a new set of experimental data making the aforementioned understanding feasible. More precisely, we will develop the micromechanics of porous baghdadite scaffolds [11] – these materials showed an in vivo osteoconductivity in critically sized defects induced into rabbit radius bones, which exceeds that of other scaffold types [12]. These developments will be described in the remainder of the present paper, which is organized as follows: porosity and ultrasonic test protocols together with their theoretical foundations will be dealt with in Section 2.1. For a deeper understanding of the resulting porosity–elasticity relations, Section 2.2 will cover a micromechanics formulation valid for a multitude of porous polycrystals, as developed in recent years [13–15], and its application to the newly collected experimental data. This will give access to the elastic properties of pure (dense) baghdadite. The methods section is then completed by a nanoindentation campaign allowing for an

\* Corresponding author.

E-mail address: [christian.hellmich@tuwien.ac.at](mailto:christian.hellmich@tuwien.ac.at) (C. Hellmich).

independent check of elasticity of pure baghdadite, as described in Section 2.3. The results of our comprehensive and consistent experimental–theoretical–computational multiscale mechanics approach to baghdadite scaffolds for bone tissue engineering are presented in Section 3, and further discussed in Section 4, in particular with respect to important theoretical and experimental features which allow for this consistent, unified view on the investigated bone biomaterial class.

## 2. Materials and methods

### 2.1. Weighing and ultrasonic tests, for porosity and elasticity determination

Combining the sol–gel method for powder production with the polymer sponge replication method for the final scaffold processing [12], cylindrically shaped porous baghdadite samples of nominally 12 mm height and 6 mm diameter were made, and categorized with decreasing nominal porosities, into sample sets A to D. Their precise dimensions of height and diameter were measured by means of a digital sliding caliper, and these dimensions were used to compute the cylindrical volume  $V$  of each of the samples. Then, their mass  $m$  was weighed, giving access to the samples' mass density through

$$\rho = m/V. \quad (1)$$

Additional consideration of the (real) mass density of pure (dense) baghdadite,  $\rho_{solid} = 3.48 \text{ g/cm}^3$  [16], allows for computation of the scaffold porosity as

$$\phi^{exp} = (1 - \rho/\rho_{solid}). \quad (2)$$

Thereafter, ultrasonic tests were performed in the pulse transmission mode, by means of a device consisting of a pulser receiver (5077PR, OlympusNDT), an oscilloscope (Waverunner 62Xi, Lecroy), and ultrasonic transducers. Following the protocol of [17,18] the pulser unit was set to emit an electrical square pulse up to 400 V. The piezoelectric elements inside the ultrasonic transducers transformed the electrical signals of a frequency  $f$  into corresponding mechanical signals, when operating in the sending mode, or they transformed mechanical signals back into electrical ones, when functioning as a receiver. Honey was used as a coupling medium. The time of flight  $t$  of the ultrasonic wave through the sample was accessed by the oscilloscope, and the travel distance through the specimen was equivalent to the scaffold's height  $h_s$ . These quantities provide direct access to the wave velocity  $v$  through

$$v = h_s/t. \quad (3)$$

According to the theory of plane waves in a 3D solid [19], the wave velocity gives access to the stiffness of the tested sample. The current study is restricted to longitudinal waves, where the directions of 'particle' displacement and of the wave propagation are parallel – in this case, the wave velocity gives access to the normal component  $C_{1111}^{exp}$  of the stiffness tensor, through

$$C_{1111}^{exp} = \rho v^2. \quad (4)$$

**Table 1**

Coefficients  $a^*$  and  $b^*$  defining linear relation (9) between Poisson's ratio of single crystals,  $\nu_s$ , and polynomial coefficients  $A_v$ ,  $B_v$ ,  $C_v$ ,  $D_v$ , and  $E_v$  in porosity–Poisson's ratio relation (8).

$q$	$a^*$	$b^*$
$A_v$	−1.0521	0.2197
$B_v$	2.2684	−0.4645
$C_v$	−0.8121	0.1662
$D_v$	0.3602	−0.0718
$E_v$	0.2394	0.1496

**Table 2**

Polishing protocol with machine PM5 Logitech (Scotland).

Step	Particle size of sandpaper [ $\mu\text{m}$ ]	Polishing time [min]	Type of arm movement	Plate speed [rpm]
1	6.5	3	Sweeping	18
2	2.5	5	Sweeping	25

What still needs to be specified is the size at which the aforementioned 'particle' is defined. In continuum (micro) mechanics [20], such a 'particle' is called material volume or representative volume element (RVE), with a characteristic length  $l_{RVE}$  being considerably larger than the inhomogeneities  $d$  within the RVE, and the RVE being subjected to homogeneous stress and strain states. Consequently, the characteristic length  $l_{RVE}$  needs to be much smaller than the scale of the characteristic loading of the medium, here the wavelength  $\lambda$ , which follows from wave velocity  $v$  and frequency  $f$  as

$$\lambda = v/f. \quad (5)$$

The aforementioned separation of length scales reads mathematically as

$$d \ll l_{RVE} \ll \lambda. \quad (6)$$

Accordingly, ultrasonic waves with wavelength  $\lambda$  detect the stiffness of a material with characteristic length  $l_{RVE}$ . More precisely, the ' $\ll$ ' signs in Eq. (6) need to refer to a ratio of  $d/\lambda \leq 0.03$ , in order to access the normal stiffness component  $C_{1111}$  of the tested material with inhomogeneity size  $d$ , as was experimentally quantified in [18]. As for the aforementioned baghdadite samples, the inhomogeneity size relates to the pore diameters, amounting to about 500  $\mu\text{m}$ , as accessed by scanning electron microscopy [12]. Thereby, the sample needs to be always representative of the material (i.e. it needs to consist of at least one entire RVE of the latter), so that  $(h_s, d_s) \geq l_{RVE}$ . Hence, the required scale separation between RVE-length and wavelength  $\lambda$  might well accomodate wavelengths which are much larger than the sample, while precisely delivering the elastic properties of the material making up the sample. In order to check different options for the determination of  $C_{1111}^{exp}$  according to Eq. (4), while considering scale separation conditions (6), the samples were sonified with a frequency of 0.1 MHz.

**Table 3**

Number of nanoindentation measurements per sample and per load.

Sample	Porosity [%]	Maximum load [mN]	Measurements
A2	94	10	22
		10	56
A8		15	39
		20	33
B8	85	10	50
		15	50
		20	50
		30	50
C3	81	10	50
		15	50
		20	50
		30	50
D1	66	10	300
		15	300
		20	300
		30	300

## 2.2. Polycrystal micromechanics–elastic properties of pure (dense) baghdadite

The porosity–stiffness relations determined experimentally according to Section 2.1 were then evaluated within the framework of continuum micromechanics (or random homogenization [20,21]) of porous polycrystals, developed in recent years for RVEs consisting of one porous phase and infinitely many, disc- or needle-shaped crystal phases oriented in different space directions [13–15]. More specifically, a large number of porosity and stiffness data from different isotropic materials, such as hydroxyapatite [22–25], bioactive glass-ceramics (CEL2) [26], gypsum [27–32], various piezoelectric ceramics [33], alumina [34–36], zirconia [36], as well as silica and nitride carbides [37–39], could be integrated into only *two* crystal shape- (i.e. needle- or disc-) specific scaling relations for the (homogenized) Young modulus of polycrystals. Both relations can be approximated by a power function reading as [15]

$$\frac{E^{hom}}{E_s} \cong B_E (1-\phi)^{C_E} \quad (7)$$

with  $E^{hom}$  as the Young modulus of the overall porous polycrystal,  $E_s$  as the Young modulus of the single crystal, and  $B_E$  and  $C_E$  as crystal shape-specific coefficients. Earlier obtained images [12] suggest the baghdadite crystals to be disc-shaped, with corresponding coefficients  $B_E = 0.9867$  and  $C_E = 2.053$  [15], and an overall Poisson ratio which only depends on that of the single crystals,  $\nu_s$ , and on the porosity  $\phi$ , following a polynomial approximation

$$\nu^{hom} = A_\nu (1-\phi)^4 + B_\nu (1-\phi)^3 + C_\nu (1-\phi)^2 + D_\nu (1-\phi) + E_\nu \quad (8)$$

with the coefficients fulfilling a linear relation of the format

$$q = a^* \nu_s + b^*, \text{ with } q = A_\nu, B_\nu, C_\nu, D_\nu, E_\nu \quad (9)$$

see Table 1 for values of  $a^*$  and  $b^*$ . Young's modulus and Poisson's ratio give access to the stiffness component  $C_{1111}$ , whereby  $E_s$  and  $\nu_s$  follow the scaling relations in Eqs. (7) and (8), so that

$$C_{1111}^{hom} = \frac{E^{hom}(E_s, \phi) \times [1 - \nu^{hom}(\nu_s, \phi)]}{[1 + \nu^{hom}(\nu_s, \phi)] \times [1 - 2\nu^{hom}(\nu_s, \phi)]} \quad (10)$$

Minimizing the mean absolute error between the micromechanics-based stiffness expression (10) evaluated for experimentally determined porosities  $\phi_i^{exp}$ , and corresponding experimentally determined stiffness values  $C_{1111}^{exp, i}$ ,

$$\sum_i |C_{1111}^{hom}(\phi_i^{exp}, E_s, \nu_s) - C_{1111}^{exp, i}| \rightarrow \min \quad (11)$$

provides an estimate for the elastic properties of pure (dense) baghdadite.

## 2.3. Nanoindentation

In order to provide a check for the estimated properties of pure baghdadite, according to Section 2.2, from experimentally determined porosity–stiffness relations and polycrystal micromechanics, a nanoindentation campaign comprising some 1750 indents was performed. For this purpose, one sample was chosen from each of the sample sets A to D. Following the protocol reported in [40], these samples were then embedded in resin (Epofix, Struers, Denmark), and held for 10 minutes in a vacuum chamber to eliminate air bubbles, before being dried for 48 h. Afterwards, the embedded samples were cut into 2 mm thick sections by means of a water-cooled low speed saw (IsoMet, Buehler),

and glued onto object slides. This enabled subsequent polishing, first through a polishing machine (PM5, Logitech, Scotland) with increasingly fine sandpaper, and eventually, with a napped cloth impregnated with 3  $\mu$ m small diamond grains, see Table 2 for details of the polishing protocol. Due to their high porosity, the samples from set A displayed very limited solid surfaces for testing. Therefore, two scaffolds from this set were prepared for nanoindentation, in order to allow for a sufficient number of measurements. The nanoindentation tests (Nano Hardness Tester, CSM, Switzerland) were performed with a Berkovich tip in the load-controlled mode. The loading–unloading rate was set at 30 mN/min, the holding time was 10 s, and four different maximum loads were used: 10, 15, 20 and 30 mN. The specific measurement details are given in Table 3. Although two scaffolds from set A were prepared for indentation, there was still not enough surface for performing as many measurements as on samples from the other sets. Thus, no tests with a maximum load of 30 mN were performed on sample set A. The 1750 measurements were evaluated according to the method of Oliver and Pharr [41], which states that the elastic unloading stiffness  $S$  is defined as the slope of the unloading curve during the initial stages of unloading. The relationship between the stiffness  $S$ , the contact area  $A$ , and the reduced elastic modulus  $E_r$  is given by

$$S = \frac{2}{\sqrt{\pi}} E_r \sqrt{A} \quad (12)$$

The reduced modulus  $E_r$  takes into account that elastic displacements occur in both the substrate – here a dense (pure) baghdadite

**Table 4**

Weight, dimensions, mass density, and porosity of tested baghdadite samples.

Sample	$m$ [g]	$h_s$ [cm]	$d_s$ [cm]	$V$ [cm <sup>3</sup> ]	$\rho$ [g/cm <sup>3</sup> ]	$\phi$ [%]
A1	0.108	1.27	0.656	0.431	0.251	93
A2	0.077	1.24	0.598	0.347	0.222	94
A3	0.127	1.20	0.625	0.369	0.344	90
A4	0.108	1.26	0.611	0.370	0.292	92
A5	0.111	1.29	0.627	0.399	0.278	92
A6	0.103	1.17	0.670	0.411	0.251	93
A7	0.132	1.27	0.616	0.379	0.348	90
A8	0.076	1.19	0.607	0.344	0.221	94
B1	0.142	1.30	0.603	0.372	0.382	89
B2	0.154	1.27	0.652	0.425	0.363	90
B3	0.151	1.26	0.638	0.404	0.374	89
B4	0.142	1.34	0.620	0.407	0.349	90
B5	0.195	1.36	0.617	0.409	0.477	86
B6	0.134	1.20	0.630	0.374	0.358	90
B7	0.146	1.27	0.630	0.396	0.368	89
B8	0.211	1.34	0.628	0.416	0.507	85
B9	0.133	1.24	0.637	0.397	0.335	90
B10	0.197	1.34	0.649	0.446	0.441	87
B11	0.126	1.21	0.633	0.381	0.330	91
C1	0.24	1.26	0.628	0.393	0.611	82
C2	0.244	1.32	0.608	0.385	0.634	82
C3	0.274	1.21	0.656	0.409	0.669	81
C4	0.236	1.31	0.642	0.427	0.553	84
C5	0.274	1.26	0.681	0.461	0.595	83
C6	0.282	1.28	0.618	0.386	0.731	79
C7	0.215	1.16	0.618	0.349	0.616	82
C8	0.267	1.30	0.664	0.450	0.593	83
C9	0.219	1.29	0.637	0.414	0.529	85
C10	0.221	1.28	0.645	0.418	0.528	85
D1	0.520	1.34	0.657	0.457	1.138	67
D2	0.484	1.25	0.656	0.423	1.144	67
D3	0.456	1.24	0.641	0.402	1.134	67
D4	0.508	1.33	0.662	0.458	1.110	68
D5	0.453	1.24	0.649	0.412	1.100	68
D6	0.430	1.17	0.675	0.420	1.024	71
D7	0.419	1.20	0.675	0.432	0.969	72
D8	0.504	1.23	0.659	0.422	1.195	66

crystal with elastic modulus  $E_s$  and Poisson's ratio  $\nu_s$  – and in the Berkovich indenter, with elastic modulus  $E_i$  and Poisson's ratio  $\nu_i$ ,

$$\frac{1}{E_r} = \frac{(1-\nu_i^2)}{E_i} + \frac{(1-\nu_s^2)}{E_s}. \quad (13)$$

The elastic properties of the diamond indenter are known and considered in the indentation software:  $E_i = 1141$  GPa and  $\nu_i = 0.07$  [41, 42]. Hence, combination of Eqs. (12) and (13) allows for expressing the Young modulus of pure baghdadite as a function of the unloading stiffness  $S$ , and of  $E_i$ ,  $\nu_i$ , and  $\nu_s$ ,

$$E_s = \frac{(1-\nu_s^2) \frac{S\sqrt{\pi}}{2\sqrt{A}} E_i}{E_i - (1-\nu_i^2) \frac{S\sqrt{\pi}}{2\sqrt{A}}} \quad (14)$$

where the value for  $\nu_s$  is adopted from the results corresponding to Section 2.2. Analysis of 1750 values for  $E_s$  according to Eq. (14) follows the concept of the statistical or grid nanoindentation method [43–45]. This method is based on the statistical analysis of a large number of indentation-derived values of a mechanical property such as Young's modulus  $E_s$ . In more detail, the measured data are first used to generate the experimental Cumulative Distribution Function (CDF): The number of indentations  $N$  and the sorted values of elastic modulus  $E^{NI}$  deliver the  $N$  points  $D_{E_s}$  of the experimental CDF,

$$D_{E^{NI}}(E_i^{NI}) = \frac{i}{N} - \frac{1}{2N} \quad (15)$$

with  $i \in [0, N]$ ,  $N = 1750$  denoting the number of indentations. The key premise of the statistical indentation method is then to approximate the experimental CDF by the superposition of several CDFs related to the individual material phases making up the substrate which is subjected to grid nanoindentation. While earlier applications of the method discriminated the material phases according to their different chemical natures [43–45], we here consider different mechanical properties arising from changes induced in the substrate material through the indentation testing itself: The loads which the substrate is subjected to, are likely to sometimes induce cracking (or damage) of the material, a phenomenon which is known to occur also in the context of nanoindentation of bone with a protocol similar to ours, see e.g. [46]. This implies that at least two material phases are expected in the tested substrate: (i) intact baghdadite, and (ii) one damaged phase (or several different damaged phases related to different crack sizes or densities, representing somehow the 'fractal' nature of cracking).

After representing the mechanical effect of all the phases by means of Gaussian (cumulative) distributions

$$D(E^{NI}, \mu_j, s_j) = \frac{1}{s_j(2\pi)^{0.5}} \int_{-\infty}^{E^{NI}} \exp\left(-\frac{(u-\mu_j)^2}{2s_j^2}\right) du \quad (16)$$

with the mean value  $\mu_j$  and standard deviation  $s_j$  of each phase, we fit the experimental CDF by  $n$  model CDFs with weighting factors (or volume fractions)  $f_j$ ,  $\sum_{j=1}^n f_j = 1$ , through minimization of the following error

$$\varepsilon = \sum_{i=1}^N \left( \sum_{j=1}^n f_j D(E_i^{NI}, \mu_j, s_j) - D_{E^{NI}}(E_i^{NI}) \right)^2 \rightarrow \min. \quad (17)$$

The minimization procedure itself is performed by an evolutionary strategy, as described in Appendix A. We realize this optimization procedure for different numbers of phases, and we check whether the number of chosen phases,  $n \geq 2$ , has an effect on the mean value of the rightmost CDF (relating to the Young's modulus of pure, intact

**Table 5**

Results of ultrasonic tests on baghdadite samples: time of flight  $t_f$ , height  $h_s$ , wave velocity  $v$ , wavelength  $\lambda$ , mass density  $\rho$ , and normal stiffness component  $C_{1111}^{exp}$ .

Sample set	$t_f$ [s]	$h_s$ [cm]	$v$ [km/s]	$\lambda$ [cm]	$\rho$ [g/cm <sup>3</sup> ]	$C_{1111}^{exp}$ [GPa]
	Measured		Eq. (3)	Eq. (5)	Eq. (1)	Eq. (4)
A1	$5.89 \times 10^{-6}$	1.27	2.16	2.16	0.251	1.17
A2	$8.84 \times 10^{-6}$	1.23	1.40	1.40	0.222	0.43
A3	$6.95 \times 10^{-6}$	1.20	1.73	1.73	0.344	1.03
A4	$6.72 \times 10^{-6}$	1.26	1.88	1.88	0.292	1.03
A5	$6.36 \times 10^{-6}$	1.29	2.03	2.03	0.278	1.15
A6	$6.36 \times 10^{-6}$	1.16	1.83	1.83	0.251	0.84
A7	$5.92 \times 10^{-6}$	1.27	2.15	2.15	0.348	1.61
A8	$7.45 \times 10^{-6}$	1.19	1.60	1.60	0.221	0.56
B1	$6.46 \times 10^{-6}$	1.30	2.01	2.01	0.382	1.55
B2	$5.61 \times 10^{-6}$	1.27	2.26	2.26	0.363	1.86
B3	$5.77 \times 10^{-6}$	1.26	2.19	2.19	0.374	1.79
B4	$5.35 \times 10^{-6}$	1.34	2.52	2.52	0.349	2.21
B5	$5.60 \times 10^{-6}$	1.36	2.44	2.44	0.477	2.84
B6	$5.74 \times 10^{-6}$	1.20	2.09	2.09	0.358	1.56
B7	$5.51 \times 10^{-6}$	1.27	2.30	2.30	0.368	1.96
B8	$5.85 \times 10^{-6}$	1.34	2.30	2.30	0.507	2.67
B9	$5.45 \times 10^{-6}$	1.24	2.29	2.29	0.335	1.75
B10	$5.54 \times 10^{-6}$	1.34	2.43	2.43	0.441	2.62
B11	$6.58 \times 10^{-6}$	1.21	1.84	1.84	0.330	1.12
C1	$4.74 \times 10^{-6}$	1.26	2.67	2.67	0.611	4.36
C2	$4.83 \times 10^{-6}$	1.32	2.74	2.74	0.634	4.76
C3	$4.03 \times 10^{-6}$	1.21	3.00	3.00	0.669	6.02
C4	$5.63 \times 10^{-6}$	1.31	2.34	2.34	0.553	3.03
C5	$4.95 \times 10^{-6}$	1.26	2.55	2.55	0.595	3.87
C6	$4.87 \times 10^{-6}$	1.28	2.64	2.64	0.731	5.09
C7	$5.12 \times 10^{-6}$	1.16	2.27	2.27	0.616	3.18
C8	$5.59 \times 10^{-6}$	1.30	2.32	2.32	0.593	3.20
C9	$5.62 \times 10^{-6}$	1.29	2.31	2.31	0.529	2.82
C10	$5.05 \times 10^{-6}$	1.28	2.53	2.53	0.528	3.39
D1	$3.69 \times 10^{-6}$	1.34	3.65	3.65	1.138	15.13
D2	$3.28 \times 10^{-6}$	1.25	3.81	3.81	1.144	16.57
D3	$3.36 \times 10^{-6}$	1.24	3.70	3.70	1.134	15.53
D4	$3.54 \times 10^{-6}$	1.33	3.76	3.76	1.110	15.65
D5	$3.26 \times 10^{-6}$	1.24	3.82	3.82	1.100	16.04
D6	$3.66 \times 10^{-6}$	1.17	3.20	3.20	1.024	10.48
D7	$3.11 \times 10^{-6}$	1.20	3.88	3.88	0.969	14.61
D8	$3.25 \times 10^{-6}$	1.23	3.80	3.80	1.195	17.27

baghdadite  $\max(\mu_j) = E_s^{NI}$ ), and whether the latter agrees with that obtained according to Section 2.2. This potential agreement is quantified through the coefficient of determination  $R^2$ , and through the relative error  $e_{rel}$  in %, which is defined as

$$e_{rel} = 100 \times \sum_{i=1}^N \left[ 1 - \frac{\sum_{j=1}^n f_j D(E_i^{NI}, \mu_j, s_j)}{D_{E^{NI}}(E_i^{NI})} \right]. \quad (18)$$

### 3. Results

#### 3.1. Porosity and elasticity determination

The porosity of the baghdadite samples ranged between 66% and 94%, see Table 4 for sample set-specific details. The corresponding normal stiffness components  $C_{1111}^{exp}$  ranged from 0.98 to 15.16 GPa, see

**Table 6**

Porosity and stiffness per sample set: mean values and standard deviations.

Sample	$\phi$ [%]	$C_{1111}^{exp}$ [GPa]
A	$92 \pm 1$	$0.98 \pm 0.34$
B	$89 \pm 2$	$1.99 \pm 0.51$
C	$83 \pm 2$	$3.97 \pm 1.00$
D	$68 \pm 2$	$15.16 \pm 1.93$



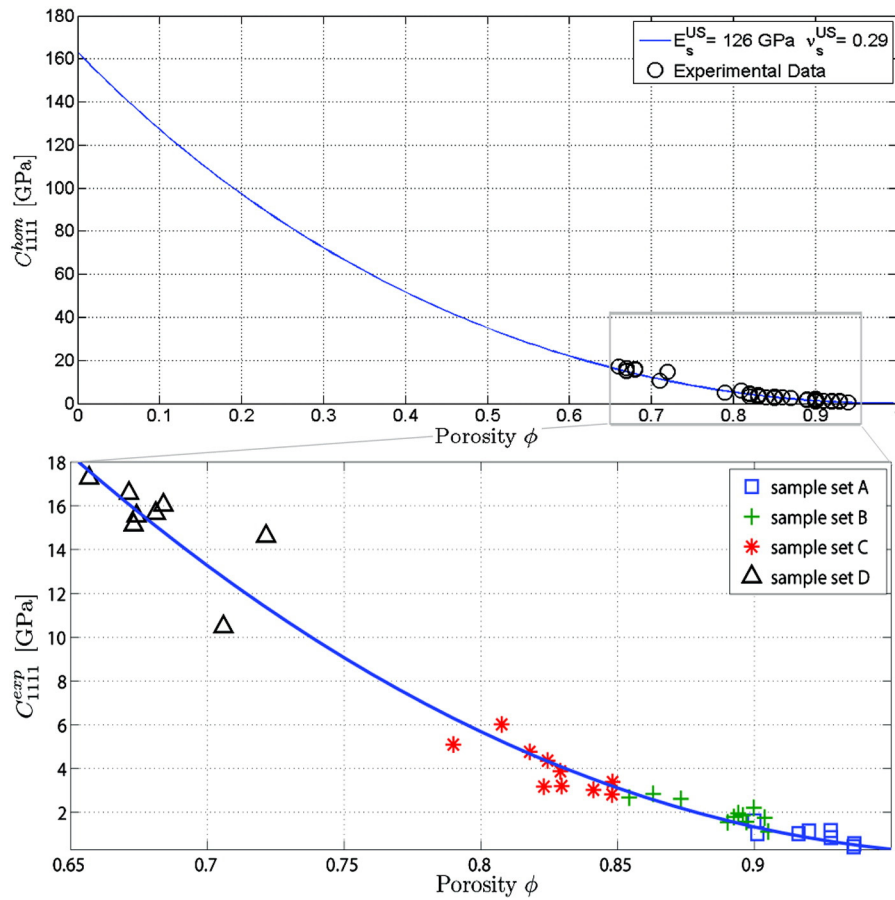


**Fig. 1.** Porosity-stiffness relation for porous baghdadite scaffolds, from optimizing micromechanics model response [15] for length measuring, weighing, and ultrasonic test results of Table 4 and 5 (experimental values are discriminated per sample set in the lower inset); this optimization provides elastic properties of pure (dense) baghdadite, and the stiffness increases with decreasing porosity.

**Table 5.** These stiffness components monotonously decrease with increasing porosity, see Table 6 and Fig. 1. The corresponding wavelengths according to Eq. (5) with  $f = 0.1$  MHz and  $\nu$  as reported in Table 5, ranged from 1.40 to 3.88 cm, hence, they fulfill the separation of scales requirement given in Eq. (6) for  $d = 500$   $\mu\text{m}$ , and, correspondingly, the derived stiffness values ranging from 0.43 to 17.27 GPa indeed refer to the overall porous baghdadite scaffold material.

### 3.2. Elastic properties of pure (dense) baghdadite

The aforementioned stiffness–porosity relation can be very well predicted by the micromechanics model of Eqs. (7)–(10): The optimization procedure (11) resulted in a fit characterized by a relative error  $e_{rel} = -4.12\%$  and a coefficient of determination  $R^2 = 0.98$ , see Fig. 1. The corresponding elastic properties of pure (dense) baghdadite

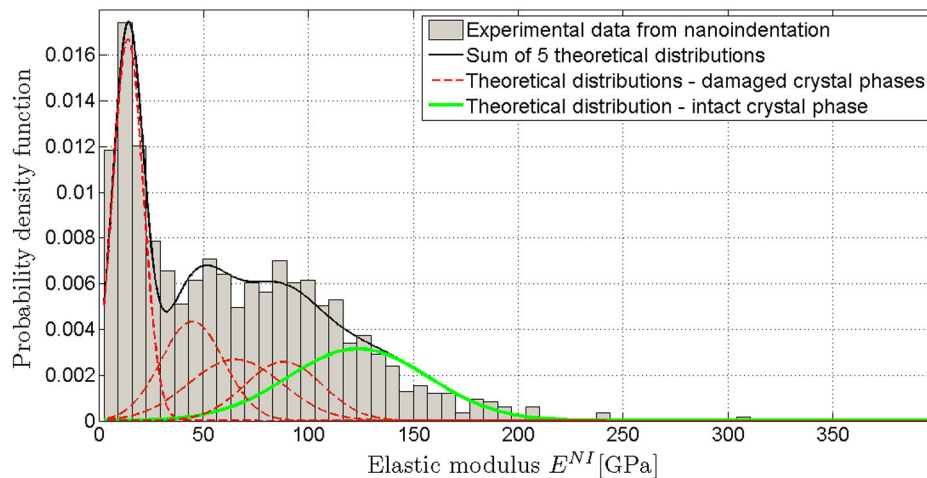


**Fig. 2.** Histogram of elastic moduli obtained from nanoindentation measurements and representation through contribution of five material phases, the stiffest of which is pure (non-damaged) baghdadite.

**Table 7**

Superposition results of  $n$  Gaussian distributions fitted to the experimental CDF which was obtained from 1750 nanoindentation measurements of baghdadite substrate; values of Young's modulus  $E_s^{NI}$ , weighting factor  $f_j$ , and the goodness of fit measurements refer to the rightmost distribution.

$n$ distributions	$E_s^{NI}$ [GPa]	$f_j$ [%]	$R^2$	$e_{rel}$ [%]
2	124.2	37.52	0.8821	−27.810%
3	127.4	26.99	0.9547	8.780%
4	122.5	27.97	0.9917	2.130%
5	123.7	26.38	0.9993	0.006%
6	127.2	32.76	0.9941	−1.530%
7	126.6	24.67	0.9531	−3.724%
8	125.6	23.65	0.9682	−1.634%
9	125.9	21.85	0.9854	−1.373%
10	126.0	20.15	0.9569	−2.921%

amounted to  $E_s = 126$  GPa and  $\nu_s = 0.29$ . Their reliability is expressed through a comparison with the 1750 results from the nanoindentation campaign, depicted in the form of a (normalized) histogram in Fig. 2. They are virtually optimally represented by a superposition of five Gaussian distribution functions, relating to a relative error amounting to only 0.006%, and a correlation coefficient of  $R^2 = 99.9\%$ , see Table 7. It is clearly seen in this table that, for up to five Gaussian distributions, the relative error decreases and the coefficient of determination increases with increasing numbers of distributions, while again higher errors and lower coefficients of determination are encountered for six and more distributions. Consequently, the fit with five distributions is the best one for the nanoindentation results, as it both minimizes the relative error and maximizes the coefficient of determination. Accordingly, the corresponding black dotted line in Fig. 2 very accurately follows the trend given by the histogram columns, and an even more impressive, almost perfect match between experimental and theoretical CDFs is observed in Fig. 3. The right most Gaussian distribution relates to the non-damaged baghdadite, i.e. to the state of the solid scaffold material also expected in ultrasonically tested scaffolds. Indeed, its mean value of  $E_s^{NI} = 124$  GPa agrees almost perfectly with  $E_s = 126$  GPa obtained from the micromechanical evaluation of the ultrasonic tests. By example, a typical load–displacement curve corresponding to a nanoindented non-damaged baghdadite crystal is depicted in Fig. 4.

#### 4. Discussion

While the current state-of-the-art in mechanical characterization of biomaterials is defined by the measurement of a few selected mechanical properties in mostly standardized mechanical testing devices, we

here go a step forward, towards a unified understanding of the mechanical functioning of an entire material class – porous scaffolds for bone tissue engineering made of baghdadite – which itself turned out to be part of yet a larger material class encompassing numerous different porous (glass-) ceramic systems. In more detail, continuum micromechanics was used as a versatile theoretical and computational framework, allowing for deriving structure–property relations in the form of elasticity functions with the porosity as an argument, these functions being experimentally validated by various physically and statistically independent experiments, namely weighing, ultrasound, and nanoindentation tests. It is not the first time that such tests have been performed on biomaterials (although mechanical testing of baghdadite appears quite rarely in literature), but the consistent emergence of just one overall picture of scaffold behavior arising from all the different tests is indeed considered as something original and remarkable (the only direct relation which can be made between our newly determined Young's modulus value of pure baghdadite,  $E_s^{NI} = 124$  GPa, and data reported in the literature, concerns very recent bending tests on low porosity baghdadite scaffolds [47], revealing modulus values between 82 and 120 GPa). The aforementioned consistency of our new results critically depends on careful evaluation of experimental data, taking into account important theoretical concepts underlying the used experimental devices. In this context, the following features of our evaluation method are particularly noteworthy:

- While the sample dimensions qualify them as fairly 'thick' beams, and classical mechanical tests when driven in unloading mode [48] would certainly deliver a Young's modulus  $E$  of the tested material, it is important to remember that ultrasonic tests in most of the cases deliver the normal stiffness component  $C_{1111}$ , rather than Young's modulus. Actually, the tested beams need to be extremely slender to allow for an extensional wave to propagate along a beam-type sample, and systematic studies [18] have shown that as long as

$$A \log\left(\frac{d}{h}\right) + B \log\left(\frac{h}{\lambda}\right) \leq 1 \quad (19)$$

with  $A = -1.426$  and  $B = -0.530$ , bulk wave propagation related to a 3D solid with normal stiffness  $C_{1111}$  occurs. For all the tests reported in the present paper, the left-hand side of Eq. (19) ranged from 0.45 to 0.67, therefore all the samples behaved as 3D solids.

- Given the fact that ultrasonic tests deliver  $C_{1111}$  rather than  $E$ , they cannot be simply compared to some more or less empirical relation concerning Young's modulus, but they need to be related to a more complete description of the material behavior. In the present case,

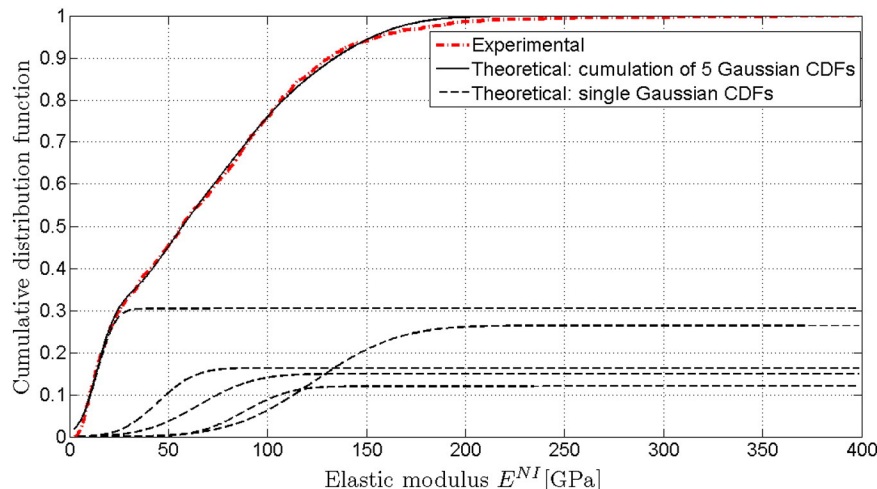


Fig. 3. Experimental CDF obtained by nanoindentation, and the five theoretical Gaussian CDFs obtained by deconvolution according to the statistical nanoindentation method of [42–44].

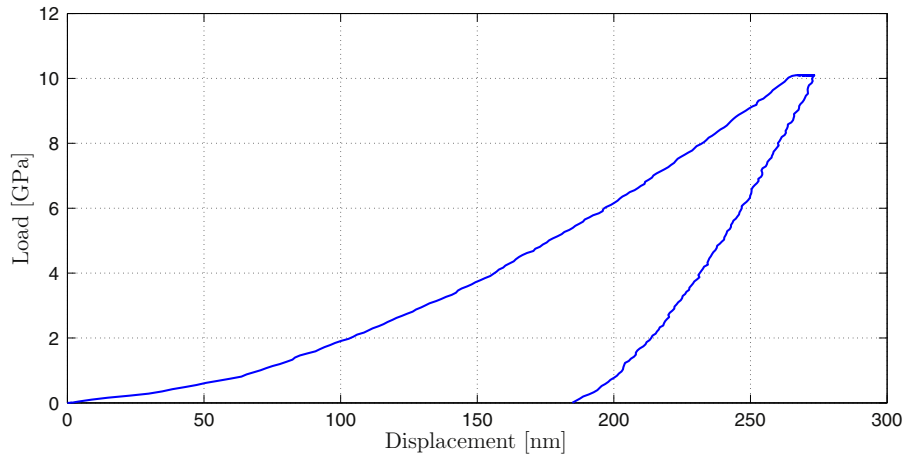


Fig. 4. Typical load–displacement curve of a non-damaged single crystal of the baghdadite scaffolds, with an obtained elastic modulus of  $E^{NI} = 124.7$  GPa at 10 mN maximal load.

this description was provided by continuum micromechanics, which delivered the full elasticity tensor. In the case of isotropic materials, as encountered here, the elasticity tensor can be expressed in terms of Young's modulus and Poisson's ratio, the latter two defining, therefore, also the stiffness component  $C_{1111}$ .

- Another critical issue with ultrasonic tests is the choice of a suitable frequency – once the corresponding wavelength does not fulfill the separation-of-scales criteria (6) anymore (a case *not* encountered here), the velocity of the ultrasonic wave is not related to the components of the elasticity tensor, i.e. ultrasound cannot be used for elasticity characterization of biomaterials anymore.
- The probably most remarkable feature of the present evaluation as compared to earlier scientific endeavors is the use and application-specific adaptation of the statistical nanoindentation method. Rather than averaging over the results of a few tests, or checking nanoindentation size effect laws [49] (see Fig. 5 for a corresponding evaluation of our nanoindentation results), which could not have provided access to the elasticity of pure (intact) baghdadite, we identified the indented substrate as being composed of one intact crystal phase and several mechanically damaged phases. This provided elastic properties which were absolutely in line with those obtained from micromechanics-based ultrasound evaluation.

Our use of micromechanics, ultrasound, and nanoindentation relates to several aspects and issues discussed in the open literature in recent

years, and the following paragraphs highlight the most important of these issues.

#### 4.1. Simple, but sufficient microelastic representation of porous baghdadite

It is noteworthy that the aforementioned successful elastic property identification rested on a relatively simple micromechanics model, which was approximated through Eq. (7), introducing just one porosity, encompassing all spaces in the material volume, except those of the dense baghdadite crystals with a mass density of  $3.48 \text{ g/cm}^3$ . However, when more closely observing scanning electron images of the tested samples, see Fig. 7(a), it becomes directly obvious that the material actually exhibits two porosity types, one with a characteristic size of  $500 \mu\text{m}$  [see Fig. 7(a)], and another one with just a few microns characteristic size [see Fig. 7(b)]. The larger pores are fully interconnected, with solid structures in between. The latter exhibit beam-, and shell-type morphologies. Zooming into the aforementioned structural elements reveals intriguing microstructures, where more disc-type, platy crystals are interconnected, so as to form a porous polycrystal [see Fig. 7(c)]. The micromechanical model approximated by Eq. (7) integrates both porosities into one “total porosity”, being related to the sum of both pore spaces divided by the total volume of the overall several millimeter-sized RVE of the investigated biomaterial. From a theoretical viewpoint, this is clearly admissible, since both pore spaces

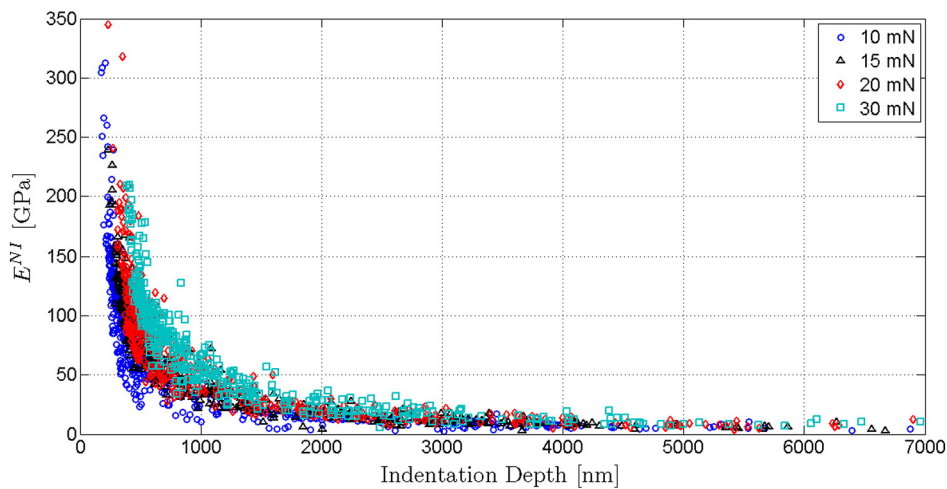


Fig. 5. Nanoindentation size effect in baghdadite scaffolds: Young's modulus  $E^{NI}$  as a function of indentation depth; experimental results are discriminated for the four investigated load levels.

exhibit lineal dimensions which are much smaller than the RVE-size, and similar mechanical properties (namely, a vanishing stiffness), so that they can be seen as just one material phase. The same holds for the solid crystals in the micrometer range: they all show comparable shapes (disc-type) and elastic properties (that of pure baghdadite), and therefore qualify as material phase in the framework of continuum micromechanics. The question on whether this quite simple micromechanical representation of the investigated (double-porous) material system is actually admissible, can only be answered through an experimental campaign: The results presented in this paper constitute indeed an impressive affirmative answer to this question. This is perhaps surprising at the first glance, but not so much at the second one, since porous baghdadite, after the present investigation, falls into a vast class of porous polycrystals given in [15], which were all very well characterizable through Eq. (7). In this context, it is noteworthy that the used micromechanics model, falling into the class of “self-consistent” models, can well represent stiffnesses of materials over the entire porosity range from 0 to 100%. This is due to the consideration of non-spherical phases, with aspect ratios going to the limit cases of “zero” or “infinity”, respectively [50,13], and this needs to be distinguished from the situation encountered with the very first self-consistent models, which were based exclusively on spherical phases [51,13]: These original models predict vanishing stiffness for a porosity larger than 50%.

#### 4.2. Separation of scales, wavelength, and ultrasonic sample size

Elastic properties are defined on so-called representative volume elements (RVEs). The latter are characterized by homogeneous boundary conditions, e.g. by boundary displacements which are related to homogeneous strains [52]. In order to allow for such homogeneous loading

conditions of the RVE, the strain fields which the structure built up by the RVEs is subjected to, need to be characterized by a phenomenological length [53],

$$\mathcal{L}_\varepsilon = \frac{\|\varepsilon\|}{\|\nabla \varepsilon\|} \quad (20)$$

which is considerably larger than the RVE,

$$\mathcal{L}_\varepsilon \gg l_{RVE}. \quad (21)$$

In Eq. (20),  $\|\cdot\|$  refers to the norm of the tensorial object ( $\cdot$ ), and the nabla-operator  $\nabla$  denotes derivatives with respect to space (spatial gradients). In addition, the RVE needs to be much larger than the characteristic inhomogeneity size  $d$  within the RVE, see Eq. (6). Targeting, in the latter context, at a few percent (say 3%) elastic homogenization error, requires the RVE to be just three times larger than the inhomogeneity size [54] – i.e.  $l_{RVE}$  approx. 1.5 mm in our case. On the other hand, ultrasonic characterization with a similar precision typically requires the wavelength to be at least five times larger than the RVE-size [17, 55], implying, in our case, wavelengths of at least 7.5 mm, a requirement clearly overfulfilled in all the ultrasonic tests performed here. Accordingly, also the difference between the two independently determined Young's moduli for pure baghdadite is only slightly more than 1%. Moreover, except for the “loading or phenomenological length scale”  $\lambda = \mathcal{L}_\varepsilon$ , no other quantity of a similar length scale enters the analysis described in the present paper. However, if one used the material properties derived here, so as to design larger constructs of porous baghdadite for large bone defect regeneration, then a structural length scale of corresponding implants,  $\mathcal{L}_s \gg l_{RVE}$  would need to come into play as well.

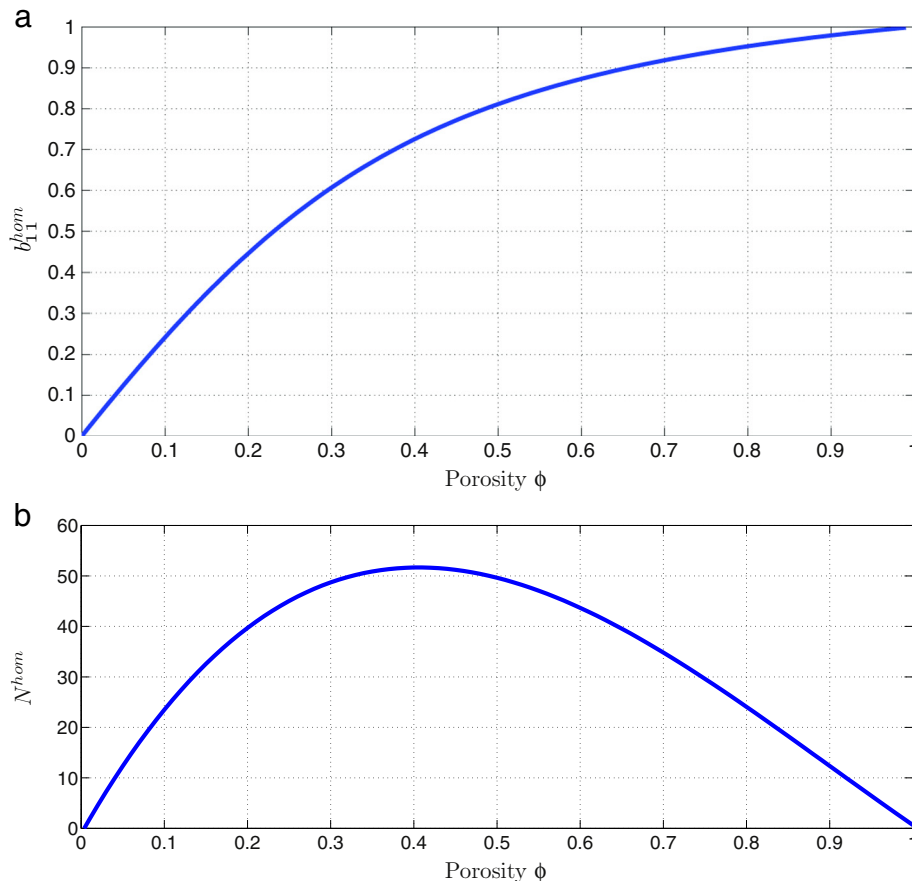


Fig. 6. Poro-elasticity of porous baghdadite scaffolds: (a) Biot coefficient as a function of porosity; (b) Biot modulus as a function of porosity.



#### 4.3. Nanoindentation: size effects, damage, and creep

It is instructive to relate the size effect shown in Fig. 5 to the microstructure appearing at the scale of corresponding indented areas, see Fig. 8. The three triangles indicated there refer to the maximum, the mean and the minimum projected indentation area  $A$ , a quantity which, for a perfect Berkovich indenter [41], is related to the indentation depth  $h_c$  by

$$A(h_c) = 24.5 h_c^2. \quad (22)$$

Also, this illustration confirms our result, given in Table 7 and Fig. 2, that only the smallest indentation sizes are related to the properties of the single crystals, while all others characterize crystal clusters with micropores and probably indentation-induced cracks in between. Accordingly, our “damaged phases” are, in fact, microporous materials (with rather small microporosity), characterized by different degrees of damage, i.e. by different (and rather substantial) microcrack densities. The latter microporosity is also probable to be (at least partially) filled by the resin used for sample preparation.

As for the indentation protocol, the holding time was introduced in order to allow for the creep of the material before unloading, thus eliminating any effect of creep in the determination of Young's modulus from the unloading curve. The characteristic time of creep  $\tau_{creep}$  was obtained from an exponential fitting of the relationship between the creep displacement rate occurred during the holding time,  $\dot{u}_{creep}$ , and the time  $t$ :

$$\dot{u}_{creep} = u_0 \exp\left(-\frac{t}{\tau_{creep}}\right), \quad (23)$$

where  $u_0$  is a constant. For the nanoindentation results referring to the pure (undamaged) baghdadite phase, the characteristic creep time amounted to  $\tau_{creep} = 2.3$  s; since 2.3 s is much less than the holding time of 10 s, we do not expect this (rather fast) creep to bias the values obtained for Young modulus related to elasticity only.

Another important issue with nanoindentation testing is the potential dependence of the obtained results on the chosen load level; often increased load levels are related to reduced on average measured elastic moduli [56]. Our rationale was not so much to reproduce this effect (which we mainly attribute to the increased damaging of the material when indenting it too strongly), but we rather targeted at finding a reasonable loading range, where at least part of the indentation campaign would be related to intact crystal characterization. In fact, the indentation loads between 10 mN and 30 mN allowed us to have loads which were high enough for reaching indentation depths beyond the roughness of the surface, and, at the same time, low enough for still obtaining results relating to non-damaged crystals [57]. Interestingly, the mean indentation depths showed no clear trend with respect to the chosen levels of 10, 15, 20 or 30 mN (see Table 8). This is consistent with the size effect relation of Fig. 5, being also independent of the chosen load level.

#### 4.4. Anisotropy effects of single baghdadite crystals

Baghdadite is a monoclinic–prismatic crystal, and therefore, in principle, anisotropic. We are not aware of any direct measurements of the full elasticity tensor of baghdadite, nor of its determination from molecular or atomistic computations. However, such data are known for other members of the monoclinic–prismatic crystal class, such as wadsleyite. The latter material was experimentally characterized by means of Brillouin light scattering [58] and its mechanical properties were computationally derived from a plane-wave pseudopotential method [59]. These methods show wadsleyite to be approximately transversely isotropic with an out-of-plane Young's modulus of  $E_0 =$

221 GPa, and a transverse Young's modulus of around  $E_T \approx 330$  GPa. Hence, the moduli in different directions vary by about  $\approx 30\%$ , a number which could also be relevant for baghdadite. As regards nanoindentation, both the lower out-of-plane and the higher in-plane Young moduli may be detected, or any value between these two extremes, depending on the crystal orientation with respect to the indentation direction. Hence, to one and the same phase (differently oriented though), many different nanoindentation-derived moduli are related, and this is exactly

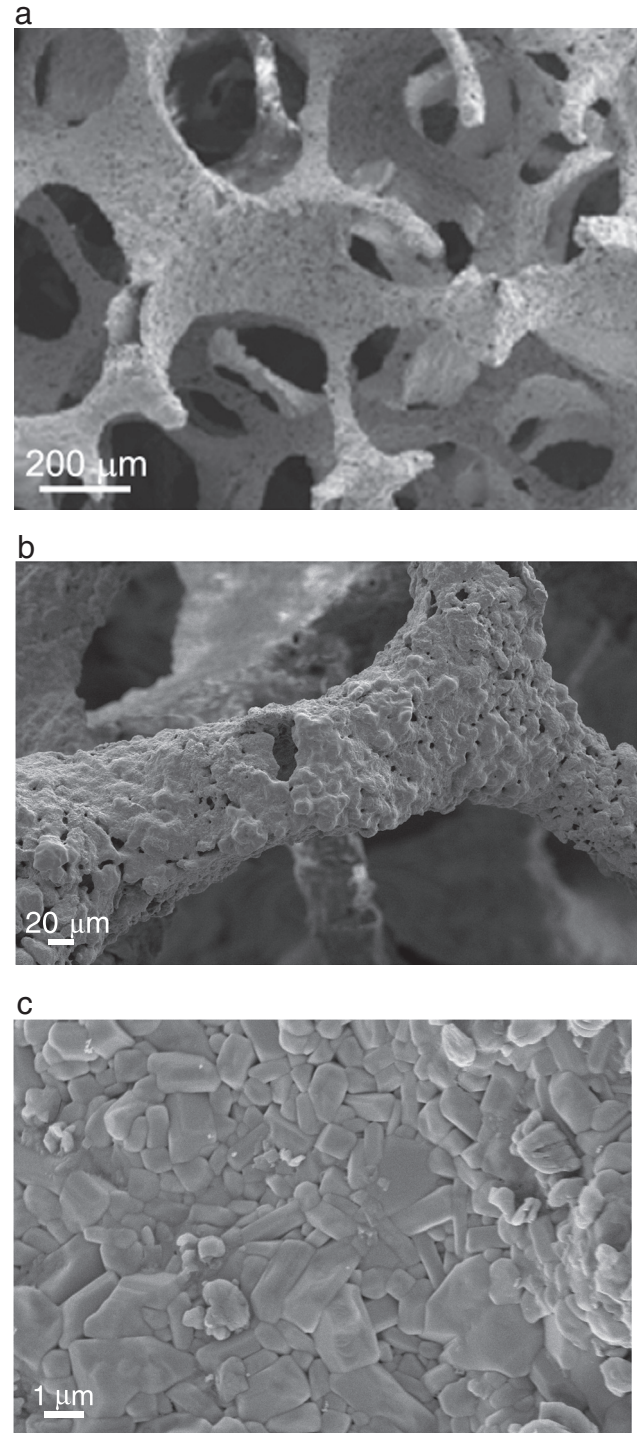


**Fig. 7.** (a) SEM image showing the macropores (black) of the baghdadite scaffolds, with beam- and shell-type structural elements in between (reproduced from Roohani-Esfahani et al. [12]); (b) SEM image showing one structural element surrounded by macroporous space; on the surface of the structural element, micropores are seen in black; (c) High-resolution SEM image of the baghdadite crystals.

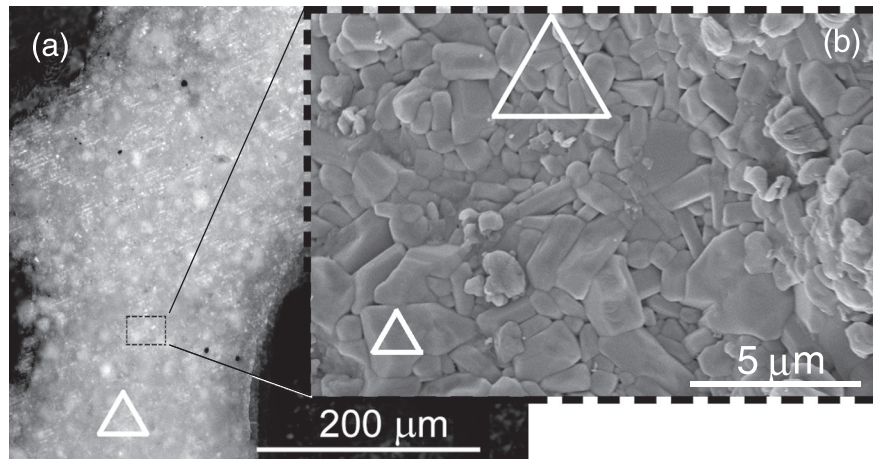


**Fig. 8.** (a) Light micrograph of polished sample surface, as prepared for nanoindentation (resin-filled macropores appear black), and (b) zoomed-out Scanning Electron Micrograph of crystalline strut surface; triangles indicate, in (a), maximum indentation size; and in (b), mean and minimum indentation sizes.

what we consider through our statistical distribution of moduli depicted in Fig. 2. More precisely, an increased difference between out-of-plane modulus and in-plane modulus would be reflected by a wider probability distribution function assigned to the respective formally isotropic phase. In this sense, the widths of all statistical distribution functions related to our differently strongly damaged phases, depicted in Fig. 2, may partially reflect the actually anisotropic nature of the tested crystals. These distribution functions also exhibit expected values, and the expected value of the undamaged phase is the Young's modulus  $E_s$  which we have been referring to throughout the present contribution. In particular, we have introduced an isotropic crystal phase exhibiting exactly this Young's modulus, so as to arrive at homogenized properties of the porous polycrystal by means of Eq. (7). The admissibility of this approximation (namely using average isotropic rather than transversely isotropic crystal properties, so as to still arrive at relevant homogenized properties of porous polycrystals) has been shown theoretically and computationally for the case of hydroxyapatite polycrystals [13].

#### 4.5. Perspectives

The herein introduced and validated micromechanics model of porous baghdadite allows for prediction of mechanical properties well beyond elasticity: In continuum micromechanics, an RVE may not only be subjected to stresses and strains at its outer boundary, but also to a pore pressure acting within the pore space. Hence, once the upscaling from the single crystal elasticity to the overall porous polycrystal is achieved, also the key poroelastic properties are known [15, 21]. They are (i) the Biot coefficient quantifying the stress arising at the undeformed boundary of the RVE, from internal pore pressure (see Fig. 6a), and (ii) the Biot modulus quantifying the porosity change within an RVE whose boundary is undeformed, again arising from pore pressure (see Fig. 6b). Equipped with this information, the elastic deformation arising from any external or internal stress states acting, under physiological conditions, on implanted porous baghdadite scaffolds can be determined. This is considered as a firm basis for computer-aided design or safety assessment of such scaffolds. In order to complete the latter, our current research activities are directed towards strength upscaling, based on the already achieved success for biomaterials made of hydroxyapatite [13–15], glass-ceramics [26], or titanium [60].

**Table 8**  
Mean value of indentation depth per load.

Load [mN]	10	15	20	30
Depth [nm]	1152	1407	1371	1458

#### Acknowledgments

Maria Pastrama and Christian Hellmich were financially supported by the European Research Council (ERC), through project ERC-2010-StG-257032-MICROBONE. The work of Hala Zreiqat and Peter Pivonka was supported by the Australian Research Council (ARC) for linkage project funding (LP0991099).

#### Appendix A. Evolutionary strategy

The evolutionary strategy [61] considers starting parameters for Gaussian distributions, namely, mean value  $\mu_0^g$ , variance  $s_0^g$ , and weighting factor  $f_0^g$ , as 'parents'  $X_p^g$ ,

$$X_p^g = \{\mu_0^g, s_0^g, f_0^g\} \quad (\text{A.1})$$

whereby the superscript  $g$  stands for the generation number, starting with  $g = 1$ . The strategy involves three subsequent steps:

##### I. Mutation

In the first step, each of these three parent values is mutated by adding a normally distributed random number,

$$X_m^g = X_p^g + Z^g \sigma \quad (\text{A.2})$$

where  $Z^g$  is generated from a normal distribution  $v(0, \sigma)$ , with mean 0 and standard deviation equal to the scattering parameter  $\alpha$ , the size of which is discussed further below. This results in a new, mutated parent, with its mutated parameters:

$$X_m^g = \{\mu_m^g, s_m^g, f_m^g\} \quad (\text{A.3})$$

##### II. Recombination

In the next step, through recombination of the starting and the mutated parameters, one obtains a series of possible combinations of parameters  $\{\mu_i^g, s_i^g, f_i^g\}$ . As the mean value and standard deviation should stem from the same group,  $i = j$ , only four combinations remain possible, out of which three are the newly generated 'offsprings',

$$\begin{aligned} X_{0,1}^g &= \{\mu_0^g, s_0^g, f_m^g\} \\ X_{0,2}^g &= \{\mu_m^g, s_m^g, f_0^g\} \\ X_{0,3}^g &= \{\mu_m^g, s_m^g, f_m^g\} \end{aligned} \quad (\text{A.4})$$



### III. Selection

In the final step, the CDF of the parent,  $CDF_p$ , and those of the offsprings,  $CDF_{Ol}$ , with  $l = 1, 2, 3$  are generated. The set of parameters that fits the data best is the one whose CDFs minimize the error given in Eq. (17). This set (either the old parent or one of the offsprings) is then selected to become the parent of the new generation  $X_p^{g+1}$ :

$$X_p^{g+1} = \{\mu_p^{g+1}, s_p^{g+1}, f_p^{g+1}\} \quad (A.5)$$

$$X_p^{g+1} = \begin{cases} X_{Ol}^g & \text{if } Error(X_{Ol}^g) < Error(X_p^g) \text{ with } l = 1, 2, 3 \\ X_p^g & \text{otherwise} \end{cases} \quad (A.6)$$

Steps I to III are repeated until a prescribed tolerance between members of subsequent generations is reached. In the current case, the set value was  $\leq |9 \cdot 10^{-5}|$ . Thus, if the first four decimals of the parameters did not change in the last 8 cycles, the most suitable distribution parameters were found. For every 10xY iterations, Y being the number of fitted parameters, the scattering factor  $\sigma$  is increased by factor  $1/\alpha$ , if the number of successful offspring selections is higher than a set threshold (in this case, 0.2 out of the 10xY iterations [62]), otherwise the factor is decreased by factor  $\alpha$ . Thereby, the step size alpha is chosen as  $\alpha = 0.85$  [62].

### References

- [1] K.U. Lewandowski, J.D. Gresser, D.L. Wise, D.J. Trantol, Bioresorbable bone graft substitutes of different osteoconductivities: a histologic evaluation of osteointegration of poly(propylene glycol-co-fumaric acid)-based cement implants in rats, *Biomaterials* 21 (8) (2000) 757–764.
- [2] G.M. Calori, E. Mazza, M. Colombo, C. Ripamonti, The use of bone-graft substitutes in large bone defects: any specific needs? *Injury* 42 (Suppl. 2) (2011) S56–S63.
- [3] J.A. Goulet, L.E. Senunas, G.L. DeSilva, M.L. Greenfield, Autogenous iliac crest bone graft. Complications and functional assessment, *Clin. Orthop. Relat. Res.* 339 (1997) 76–81.
- [4] W.R. Moore, S.E. Graves, G.I. Bain, Synthetic bone graft substitutes, *ANZ J. Surg.* 71 (6) (2001) 354–361.
- [5] R. Langer, J. Vacanti, Tissue engineering, *Science* 260 (5110) (1993) 920–926.
- [6] S.J. Hollister, Porous scaffold design for tissue engineering, *Nat. Mater.* 4 (7) (2005) 518–524.
- [7] D.W. Hutmacher, Scaffolds in tissue engineering bone and cartilage, *Biomaterials* 21 (24) (2000) 2529–2543.
- [8] L.G. Griffith, G. Naughton, Tissue engineering—current challenges and expanding opportunities, *Science* 295 (5557) (2002) 1009–1014.
- [9] Y. Bala, B. Depalle, T. Douillard, S. Meille, P. Clément, H. Follet, et al., Respective roles of organic and mineral components of human cortical bone matrix in micromechanical behavior: an instrumented indentation study, *J. Mech. Behav. Biomed. Mater.* 4 (7) (2011) 1473–1482.
- [10] R. Khanna, K.S. Katti, D.R. Katti, Experiments in nanomechanical properties of live osteoblast cells and cell–biomaterial interface, *J. Nanotechnol. Eng. Med.* 2 (4) (2012) 041005 (13 pages).
- [11] Y. Ramaswamy, C. Wu, A.V. Hummel, V. Combes, G. Grau, H. Zreiqat, The responses of osteoblasts, osteoclasts and endothelial cells to zirconium modified calcium-silicate-based ceramic, *Biomaterials* 29 (33) (2008) 4392–4402.
- [12] S.I. Roohani-Esfahani, C.R. Dunstan, B. Davies, S. Pearce, R. Williams, H. Zreiqat, Repairing a critical-sized bone defect with highly porous modified and unmodified baghdadite scaffolds, *Acta Biomater.* 8 (11) (2012) 4162–4172.
- [13] A. Fritsch, L. Dormieux, C. Hellmich, Porous polycrystals built up by uniformly and axisymmetrically oriented needles: homogenization of elastic properties, *CR Mécanique* 334 (3) (2006) 151–157.
- [14] A. Fritsch, L. Dormieux, C. Hellmich, J. Sanahuja, Mechanical behavior of hydroxyapatite biomaterials: an experimentally validated micromechanical model for elasticity and strength, *J. Biomed. Mater. Res. A* 88A (1) (2009) 149–161.
- [15] A. Fritsch, C. Hellmich, P. Young, Micromechanics-derived scaling relations for poroelasticity and strength of brittle porous polycrystals, *J. Appl. Mech.* 80 (2) (2013) 020905 (12 pages).
- [16] H.M. Al-Hermezi, D. McKie, A.J. Hall, Baghdadite, a new calcium zirconium silicate mineral from Iraq, *Mineral. Mag.* 50 (1986) 119–123.
- [17] C. Kohlhauser, C. Hellmich, C. Vitale-Brovarone, A.R. Boccacini, A. Rota, J. Eberhardsteiner, Ultrasonic characterisation of porous biomaterials across different frequencies, *Strain* 45 (1) (2009) 34–44.
- [18] C. Kohlhauser, C. Hellmich, Ultrasonic contact pulse transmission for elastic wave velocity and stiffness determination: influence of specimen geometry and porosity, *Eng. Struct.* 47 (2013) 115–133.
- [19] J.M. Carcione, *Wave Fields in Real Media: Wave Propagation in Anisotropic, Anelastic, and Porous Media*, 1st ed. Elsevier, Oxford, 2001.
- [20] A. Zaoui, Continuum micromechanics: survey, *J. Eng. Mech.* 128 (8) (2002) 808816.
- [21] L. Dormieux, D. Kondo, F.J. Ulm, *Microporomechanics*, Wiley, Chichester, 2006.
- [22] G. De With, H. Van Dijk, N. Hattut, K. Prijs, Preparation, microstructure and mechanical properties of dense polycrystalline hydroxy apatite, *J. Mater. Sci.* 16 (6) (1981) 1592–1598.
- [23] R. Gilmore, J. Katz, Elastic properties of apatites, *J. Mater. Sci.* 17 (4) (1982) 1131–1141.
- [24] D.M. Liu, Preparation and characterisation of porous hydroxyapatite bioceramic via a slip-casting route, *Ceram. Int.* 24 (6) (1998) 441–446.
- [25] E. Charrière, S. Terrazzoni, C. Pittet, P. Mordasini, M. Dutoit, J. Lemaître, et al., Mechanical characterization of brushite and hydroxyapatite cements, *Biomaterials* 22 (21) (2001) 2937–2945.
- [26] A. Malasoma, A. Fritsch, C. Kohlhauser, T. Brynk, C. Vitale-Brovarone, Z. Pakiel, et al., Micromechanics of bioresorbable porous CEL2 glass ceramic scaffolds for bone tissue engineering, *Adv. Appl. Ceram.* 107 (5) (2008) 277–286.
- [27] M. Ali, B. Singh, The effect of porosity on the properties of glass fibre-reinforced gypsum plaster, *J. Mater. Sci.* 10 (11) (1975) 1920–1928.
- [28] K. Phani, Young's modulus–porosity relation in gypsum systems, *Am. Ceram. Soc. Bull.* 65 (1986) 1584–1586.
- [29] Ei Tazawa, Effect of self stress on flexural strength of gypsum–polymer composites, *Adv. Cem. Based Mater.* 7 (1) (1998) 1–7.
- [30] S. Meille, Étude du comportement mécanique du plâtre pris en relation avec sa microstructure, (Ph.d. thesis), INSA de Lyon, 2001.
- [31] A. Colak, Physical and mechanical properties of polymer–plaster composites, *Mater. Lett.* 60 (16) (2006) 1977–1982.
- [32] J. Sanahuja, L. Dormieux, S. Meille, C. Hellmich, A. Fritsch, Micromechanical explanation of elasticity and strength of gypsum: from elongated anisotropic crystals to isotropic porous polycrystals, *J. Eng. Mech.* 136 (2) (2010) 239–253.
- [33] F. Craciun, C. Galassi, E. Roncari, A. Filippi, G. Guidarelli, Electro-elastic properties of porous piezoelectric ceramics obtained by tape casting, *Ferroelectrics* 205 (1) (1998) 49–67.
- [34] R.L. Coble, W.D. Kingery, Effect of porosity on physical properties of sintered alumina, *J. Am. Ceram. Soc.* 39 (11) (1956) 377–385.
- [35] W. Pabst, E. Gregorová, G. Tichá, E. Tynová, Effective elastic properties of alumina–zirconia composite ceramics—part 4. Tensile modulus of porous alumina and zirconia, *Ceram. Silik.* 48 (4) (2004) 165–174.
- [36] W. Pabst, E. Gregorová, G. Tichá, Elasticity of porous ceramics — a critical study of modulus–porosity relations, *J. Eur. Ceram. Soc.* 26 (7) (2006) 1085–1097.
- [37] C. Reynaud, F. Thévenot, T. Chartier, J.L. Besson, Mechanical properties and mechanical behaviour of SiC dense-porous laminates, *J. Eur. Ceram. Soc.* 25 (5) (2005) 589–597.
- [38] A. Diaz, S. Hampshire, Characterisation of porous silicon nitride materials produced with starch, *J. Eur. Ceram. Soc.* 24 (2004) 413–419.
- [39] J. Haglung, O.J. Hunter, Elastic properties of polycrystalline monoclinic  $Gd_2O_3$ , *J. Am. Ceram. Soc.* 56 (1973) 327–330.
- [40] J. Hum, K.W. Luczynski, P. Noeaid, P. Newby, O. Lahayne, C. Hellmich, et al., Stiffness improvement of 4555 bioglass®-based scaffolds through natural and synthetic biopolymer coatings: an ultrasonic study, *Strain* 49 (5) (2013) 431–439.
- [41] W. Oliver, G. Pharr, An improved technique for determining hardness and elastic modulus using load and displacement sensing indentation experiments, *J. Mater. Res.* 7 (1992) 1564–1583.
- [42] *Indentation Software User's Manual*, CSM Instruments; Rue de la Gare 4 CH-2034 Pesieux (Switzerland), 2008.
- [43] G. Constantinides, K.R. Chandran, F.J. Ulm, K.V. Vliet, Grid indentation analysis of composite microstructure and mechanics: principles and validation, *Mater. Sci. Eng. A-Struct.* 430 (2006) 189–202.
- [44] G. Constantinides, F. Ulm, The nanogranular nature of C–S–H, *J. Mech. Phys. Solids* 55 (1) (2007) 64–90.
- [45] F.J. Ulm, M. Vandamme, C. Bobko, J. Alberto Ortega, K. Tai, C. Ortiz, Statistical indentation techniques for hydrated nanocomposites: concrete, bone, and shale, *J. Am. Ceram. Soc.* 90 (9) (2007) 2677–2692.
- [46] A. Malandrino, A. Fritsch, O. Lahayne, K. Kropik, H. Redl, J. Noailly, et al., Anisotropic tissue elasticity in human lumbar vertebra, by means of a coupled ultrasound-micromechanics approach, *Mater. Lett.* 78 (2012) 154–158.
- [47] T.C. Schuhmacher, E. Volkmann, R. Yilmaz, A. Wolf, T. Treccani, K. Rezwan, Mechanical evaluation of calcium–zirconium-silicate (baghdadite) obtained by a direct solid-state synthesis route, *J. Mech. Behav. Biomed. Mater.* 34 (2014) 294–301.
- [48] K.W. Luczynski, T. Brynk, B. Ostrowska, W. Swieszkowski, R. Reihnsner, C. Hellmich, Consistent quasistatic and acoustic elasticity determination of poly-L-lactide-based rapid-prototyped tissue engineering scaffolds, *J. Biomed. Mater. Res. A* 101A (1) (2013) 138–144.
- [49] W.D. Nix, H. Gao, Indentation size effects in crystalline materials: a law for strain gradient plasticity, *J. Mech. Phys. Solids* 46 (3) (1998) 411–425.
- [50] B. Pichler, C. Hellmich, J. Eberhardsteiner, Spherical and acicular representation of hydrates in a micromechanical model for cement paste: prediction of early-age elasticity and strength, *Acta Mech.* 203 (2009) 137–162.
- [51] A.V. Hershey, The elasticity of an isotropic aggregate of anisotropic cubic crystals, *J. Appl. Mech. ASME* 21 (1954) 236–240.
- [52] Z. Hashin, Analysis of composite materials — a survey, *J. Appl. Mech.* 50 (3) (1983) 481–505.
- [53] J.L. Auriault, C. Boutin, C. Geindreau, Homogenization of Coupled Phenomena in Heterogeneous Media, Wiley, 2009.
- [54] W.J. Drugan, J.R. Willis, A micromechanics-based nonlocal constitutive equation and estimates of representative volume element size for elastic composites, *J. Mech. Phys. Solids* 44 (1996) 497–524.

- [55] S. Scheiner, R. Sinibaldi, B. Pichler, V. Komlev, C. Renghini, C. Vitale-Brovarone, F. Rustichelli, C. Hellmich, Micromechanics of bone tissue-engineering scaffolds, based on resolution error-cleared computer tomography, *Biomaterials* 30 (2009) 2411–2419.
- [56] R. Khanna, K.S. Katti, D.R. Katti, Nanomechanics of surface modified nanohydroxyapatite particulates used in biomaterials, *J. Eng. Mech.* 135 (5) (2009) 468–478.
- [57] C. Bobko, F.-J. Ulm, The nano-mechanical morphology of shale, *Mech. Mater.* 40 (2008) 318–337.
- [58] H. Sawamoto, D.J. Weidner, S. Sasaki, M. Kumazawa, Single-crystal elastic properties of the modified spinel (beta) phase of magnesium orthosilicate, *Science* 224 (4650) (1984) 749–751.
- [59] B. Kiefer, L. Stixrude, J. Hafner, G. Kresse, Structure and elasticity of wadsleyite at high pressures, *Am. Mineral.* 86 (2001) 1387–1395.
- [60] H.W. Müllner, A. Fritsch, C. Kohlhauser, R. Reihnsner, C. Hellmich, D. Godlinski, et al., Acoustical and poromechanical characterisation of titanium scaffolds for biomedical applications, *Strain* 44 (2) (2008) 153–163.
- [61] M. Jaendl, A. Reinbacher-Köstinger, C. Magele, W. Renhart, Multi-objective optimization using evolution strategies, *Electron. Energetics* 22 (2) (2009) 159–174.
- [62] K. Weicker, *Evolutionäre Algorithmen. Leitfaden der Informatik*, Vieweg+Teubner Verlag, 2007.